

# PROCEEDINGS OF SPIE

[SPIDigitalLibrary.org/conference-proceedings-of-spie](https://spiedigitallibrary.org/conference-proceedings-of-spie)

## Towards the experimental validation of the non-linear dark hole on the THD bench

Olivier Herscovici-Schiller, Laurent M. Mugnier, Pierre Baudoz, Raphaël Galicher, Jean-François Sauvage, et al.

Olivier Herscovici-Schiller, Laurent M. Mugnier, Pierre Baudoz, Raphaël Galicher, Jean-François Sauvage, Fabien Patru, Lucie Leboulleux, Arthur Vigan, Kjetil Dohlen, Thierry Fusco, Laurent Pueyo, Rémi Soummer, Jean-Michel Le Duigou, "Towards the experimental validation of the non-linear dark hole on the THD bench," Proc. SPIE 10703, Adaptive Optics Systems VI, 1070329 (12 July 2018); doi: 10.1117/12.2314100

**SPIE.**

Event: SPIE Astronomical Telescopes + Instrumentation, 2018, Austin, Texas, United States

# Towards the experimental validation of the non-linear dark hole on the THD bench

Olivier Herscovici-Schiller<sup>a</sup>, Laurent M. Mugnier<sup>a</sup>, Pierre Baudoz<sup>b</sup>, Raphaël Galicher<sup>b</sup>, Jean-François Sauvage<sup>a,c</sup>, Fabien Patru<sup>b</sup>, Lucie Leboulleux<sup>a,c,d</sup>, Arthur Vigan<sup>c</sup>, Kjetil Dohlen<sup>c</sup>, Thierry Fusco<sup>a,c</sup>, Laurent Pueyo<sup>d</sup>, Rémi Soummer<sup>d</sup>, and Jean-Michel Le Duigou<sup>e</sup>

<sup>a</sup>ONERA – The French Aerospace Lab, F-92322 Châtillon, France

<sup>b</sup>LESIA, Observatoire de Paris, PSL Research University, CNRS, Sorbonne Universités, UPMC Université Paris 06, Université Paris Diderot, Sorbonne Paris Cité 5 place Jules Janssen, 92195 Meudon, France

<sup>c</sup>Laboratoire d'Astrophysique de Marseille, UMR 7326, Aix-Marseille Université, CNRS F-13388 Marseille, France

<sup>d</sup>Space Telescope Science Institute, 3700 San Martin Drive, Baltimore, MD 21218, USA

<sup>e</sup>Centre National d'Études Spatiales, 18 Avenue Edouard Belin 31401 Toulouse cedex 9, France

## ABSTRACT

New space missions dedicated to exoplanet imaging will rely on coronagraphs to address the high contrast between the stars and their environments. In order to avoid the image of planets to be lost in post-coronagraphic starlight residuals, high precision wavefront sensing and control is a key element to these missions. We present recent results of simultaneous post-coronagraphic phase and amplitude sensing obtained on the THD bench using the coronagraphic phase diversity. We also present results of simulation studies on the non-linear dark hole technique to assess the main limitations of this technique. Finally, we present a first experimental validation of its principle and corroborate expectations on its speed of convergence. These results suggest that the non-linear dark hole is a good candidate for wave-front control for future space-based exoplanet imaging missions, where fast techniques to produce deep dark holes are of paramount importance.

**Keywords:** exoplanet imaging, coronagraph, wavefront sensing, wavefront control, coronagraphic phase diversity, non-linear dark hole

## 1. INTRODUCTION

The final performance of current and future instruments dedicated to exoplanet detection and characterization is limited by intensity residuals in the scientific image plane, which originate in uncorrected optical aberrations.

The main contribution to these residuals (after correction of turbulence by Adaptive Optics for ground-based instruments) comes from the quasi-static aberrations introduced upstream of the coronagraph, which create long-lived speckles in the detector plane that can easily be mistaken for a planet. These aberrations must be measured and compensated for.

Additionally, in order to reach the very high contrasts required to image Earth-like planets from space, two specific problems must be tackled: firstly, one must be able to measure not only phase aberrations, but also amplitude variations in the instrument's pupil, referred to as amplitude aberrations. In other words one needs to measure the complex wavefront, and this needs to be done using the scientific sensor itself in order to avoid differential aberrations between the wavefront sensor and the scientific path, a.k.a. NCPA (for Non-Common Path Aberrations).

---

Further author information:

O.H.-S.: E-mail: olivier.herscovici-schiller@onera.fr

L.M.M.: E-mail: mugnier@onera.fr

Adaptive Optics Systems VI, edited by Laird M. Close, Laura Schreiber,  
Dirk Schmidt, Proc. of SPIE Vol. 10703, 1070329 · © 2018 SPIE  
CCC code: 0277-786X/18/\$18 · doi: 10.1117/12.2314100

Secondly, one needs to control the wavefront in order to create a dark zone (a.k.a. “dark hole”) in the focal-plane area where planets are searched for, rather than to simply flatten the wavefront. Most techniques used for this purpose rely on a linearized relationship between the phase aberration produced by a deformable mirror and the intensity in the focal plane. Consequently, a number of iterations (typically several dozens) is necessary in order to reach a minimum of starlight intensity in the dark hole. Additionally, the interaction matrix, which embodies this assumed linear relationship, may have to be recalibrated several times in order to achieve a deep dark hole. These iterations and calibrations can make the whole procedure exceedingly time-consuming.

In this communication we address these two points. Firstly, in Section 2, we show that COFFEE, the coronagraphic phase diversity, can be extended to the estimation of both the phase and the amplitude aberrations, and we demonstrate this on experimental high contrast images on the THD2 (très haute dynamique version 2) bench of Observatoire de Paris.<sup>1</sup>

Secondly, we perform the first experimental proof of concept of the Non-Linear Dark Hole (NLDH) method,<sup>2</sup> which minimizes the starlight intensity in a given focal-plane area using an exact, non-linear, coronagraphic imaging model, and thus should produce the dark hole in just a few iterations. As a first preliminary validation, we experiment in Section 3.2 the NLDH technique on the MITHiC bench at Laboratoire d’Astrophysique de Marseille (LAM) without a coronagraph, and converge towards a dark hole very similar to that obtained with the Apodizing Phase Plate (APP).<sup>3</sup> Then in Section 3, we move to the THD2 bench where we perform a dark hole with the NLDH technique in the presence of a FQPM coronagraph.

## 2. SIMULTANEOUS PHASE AND AMPLITUDE WAVEFRONT SENSING WITH COFFEE ON THD

### 2.1 Formalism

#### 2.1.1 Image formation model

We consider a coronagraphic imaging system observing a point source. Let  $\exp(i\phi_u + \xi_u)$  be the complex field to be estimated in a pupil plane upstream of the coronagraph, and  $\phi_d$  the phase aberrations in a pupil plane downstream of the coronagraph. We denote by  $\mathbf{h}_c(\phi_u, \xi_u, \phi_d)$  the model of the coronagraphic PSF as a function of  $\phi_u, \xi_u, \phi_d$ —see Ref 1 for the details on the expression of  $\mathbf{h}_c$ . We assume that we record three coronagraphic images in the focal plane: one focused image  $\mathbf{i}_c^0$  and two diversity images  $\mathbf{i}_c^1$  and  $\mathbf{i}_c^2$ , differing from the focused image by a known diversity,  $\phi_{\text{div}}^1$  and  $\phi_{\text{div}}^2$  respectively. These images can be written as:

$$\mathbf{i}_c^p = \alpha_p \mathbf{h}_{\text{det}} \star \mathbf{h}_c(\phi_u + \phi_{\text{div}}^p, \xi_u, \phi_d) + \beta_p + \mathbf{n}_p. \quad (1)$$

where  $\alpha_p$  is the flux of the star in image number  $p$  ( $p \in \{0, 1, 2\}$ ),  $\beta_p$  represents a constant residual background in image  $\mathbf{i}_c^p$ ,  $\mathbf{h}_{\text{det}}$  is the detector PSF,  $\mathbf{n}_p$  denotes the measurement noise, and by convention  $\phi_{\text{div}}^0 = 0$ . The noise is usually a combination of photon and detector noises, which can be well approximated by a white Gaussian inhomogeneous noise for the flux levels at hand in high contrast imaging. Its variance is then the sum of the variances of the photon noise  $\sigma_{\text{det}_p}^2$  and of the detector noise  $\sigma_{\text{phot}_p}^2$ <sup>4</sup>:

$$\sigma_{n_p}^2[k] = \sigma_{\text{det}_p}^2 + \sigma_{\text{phot}_p}^2[k], \quad (2)$$

where  $k$  is the current pixel index. In this equation,  $\sigma_{\text{det}_p}$  is a scalar determined by the calibration of the detector, and the variance map  $\sigma_{\text{phot}_p}^2[k]$  can be estimated simply from the image  $\mathbf{i}_c^p$  itself<sup>4</sup>:

$$\sigma_{\text{phot}}^2[k] = \max(\mathbf{i}_c^p[k], 0) \quad (3)$$

#### 2.1.2 MAP metric for phase and amplitude reconstruction

The COFFEE method is based on the optimization of a Maximum *A Posteriori* (MAP) metric. It consists in searching for the upstream phase and amplitude aberrations  $\hat{\phi}_u$  and  $\hat{\xi}_u$ , the downstream phase aberrations  $\hat{\phi}_d$ , as well as the fluxes  $\hat{\alpha} = [\hat{\alpha}_0, \hat{\alpha}_1, \hat{\alpha}_2]$  and the background values  $\hat{\beta} = [\hat{\beta}_0, \hat{\beta}_1, \hat{\beta}_2]$  that maximize the posterior

likelihood  $p(\alpha, \beta, \phi_u, \xi_u, \phi_d | i_c^0, i_c^1, i_c^2)$ . In practice, the solution is obtained by the minimization of the neg-log-likelihood metric  $J$  defined as the opposite of the logarithm of this posterior likelihood, i.e.:

$$(\hat{\alpha}, \hat{\beta}, \hat{\phi}_u, \hat{\xi}_u, \hat{\phi}_d) = \arg \min_{\alpha, \beta, \phi_u, \xi_u, \phi_d} J(\alpha, \beta, \phi_u, \xi_u, \phi_d), \quad (4)$$

with:

$$J(\alpha, \beta, \phi_u, \xi_u, \phi_d) = \frac{1}{2} \sum_p \left\| \frac{i_c^p - [\alpha_p h_{\text{det}} \star h_c(\phi_u + \phi_{\text{div}}^p, \xi_u, \phi_d) + \beta_p]}{\sigma_{n_p}} \right\|^2 + \mathcal{R}(\phi_u) + \mathcal{R}(\xi_u) + \mathcal{R}(\phi_d), \quad (5)$$

where  $\mathcal{R}(\phi_q)$  represents the regularization term on the phase aberration  $\phi_q$ , with  $q \in [u, d]$ , and  $\mathcal{R}(\xi_u)$  represents the regularization term on the amplitude aberrations  $\xi_u$ . The minimization of metric  $J$  (Equation 5) is performed by means of the VMLM-B method,<sup>5</sup> and relies on the analytical expressions of gradients  $\partial J / \partial \phi_u$ ,  $\partial J / \partial \xi_u$ ,  $\partial J / \partial \phi_d$ ,  $\partial J / \partial \alpha$  and  $\partial J / \partial \beta$ .

### 2.1.3 Choice of appropriate basis and regularization for the aberrations

The use of a pixel basis for the phase reconstruction is required for COFFEE to estimate high order aberrations. However, this leads to a large number of unknowns, which in turn calls for a regularization metric in order to reduce the noise sensitivity. We chose a regularization metric that is based on the available a priori knowledge on the quasi-static aberrations. Indeed, they can be reasonably assumed to be Gaussian, homogeneous and thus endowed with a power spectral density (PSD). In this communication, we use the regularization in  $1/f^2$  whose implementation is described in Ref. 2, complemented by a regularization developed specifically for the FQPM coronagraph in order to avoid an uncontrolled amplification of the unseen modes of this particular coronagraph—see Ref 1 for details.

## 2.2 The THD2 bench

The THD2 bench is the very high contrast testbed of Observatoire de Paris. It is represented on Fig. 1,

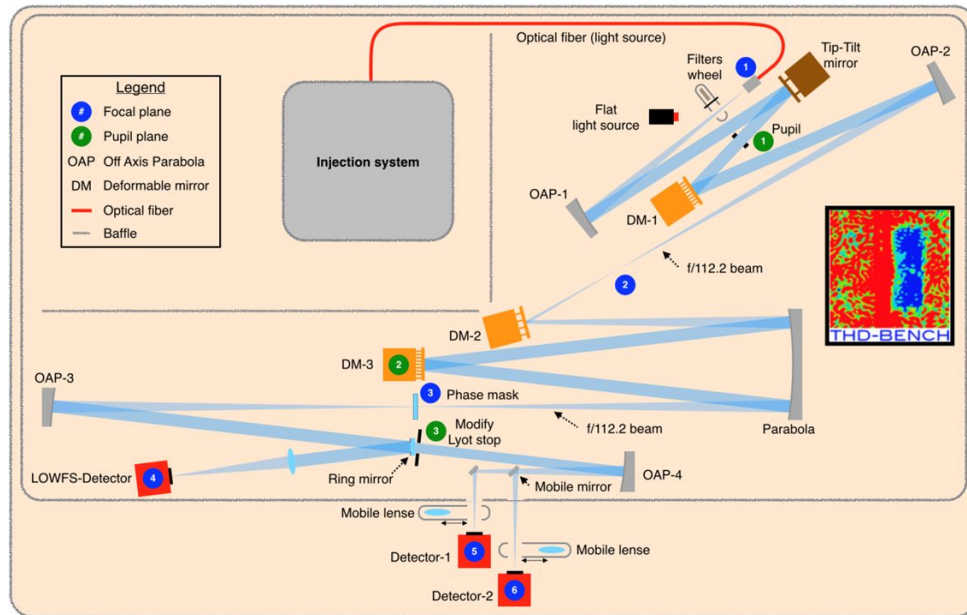


Figure 1. Optical design of the THD2 Testbed

and is schematically described in Fig. 2. We will be mostly interested in the fact that it allows for the use of:

- a monochromatic light source of wavelength 783.25 nm;
- a photometer for a precise normalization of the light flux;
- an off-pupil deformable mirror, DM1, hereafter called “amplitude mirror”;
- a pupil-plane deformable mirror, DM3, hereafter called “phase mirror”;
- a four-quadrant phase mask coronagraph;
- a camera.

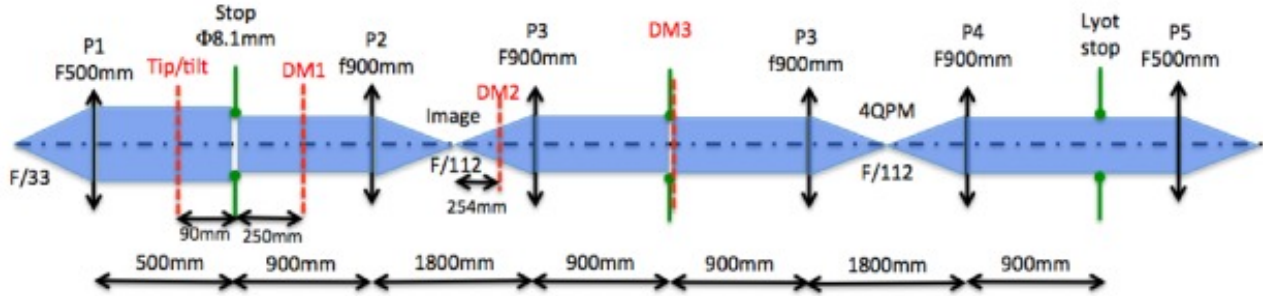


Figure 2. Schematic design of the THD2 Testbed

### 2.3 Simultaneous phase and amplitude wavefront sensing & comparison with SCC

This Section reports on the experimental validation of the joint measurement of phase and amplitude with COFFEE on the THD2 bench.

We begin by a careful calibration of the image sampling, of the Lyot stop diameter ratio, and of the diversity phases produced by the pupil-plane deformable mirror, DM3—see Ref 1 for details.

Then we perform COFFEE measurements (3 images) and wavefront reconstructions, firstly with the bench in its reference state (extremely small aberrations, leading to a  $10^{-8}$  contrast in intensity), secondly with a known wavefront mixing phase and amplitude aberrations. The difference of the two reconstructions will constitute our final wavefront estimate. Figures 3 and 4 show these two sets of images.

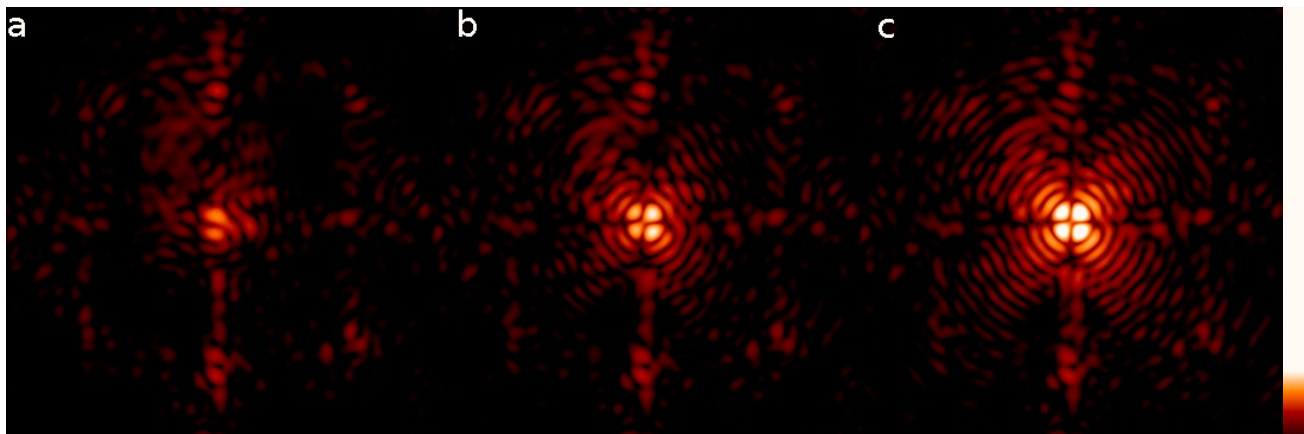


Figure 3. a. Focused image  $\mathbf{I}_{k=0}^0$  (left). b. Diversity image  $\mathbf{I}_{k=1}^0$  (middle). c. Diversity image  $\mathbf{I}_{k=2}^0$  (right). The scale is an argument hyperbolic sine, with the same color scale for all the images.

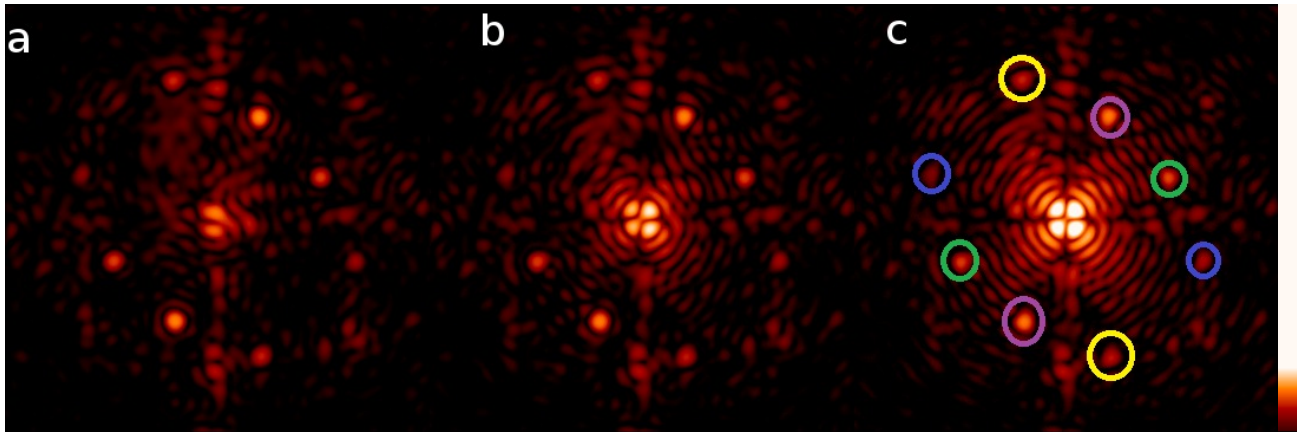


Figure 4. a. Focused image  $\mathbf{I}_{k=0}^2$  (left). b. Diversity image  $\mathbf{I}_{k=1}^2$  (middle). c. Diversity image  $\mathbf{I}_{k=2}^2$  (right). The scale is an argument hyperbolic sine. On the rightmost image, the main pair of amplitude spots is enhanced by green circles, and the corresponding replica spots are enhanced by blue circles. The main pair of phase spots is enhanced by purple circles, and the corresponding replica spots are enhanced by yellow circles. They are clearly visible in all three images.

The known wavefront mixing phase and amplitude aberrations is composed of an amplitude sinusoid and a phase sinusoid at different spatial frequencies. The amplitude sinusoid is produced by a phase on the off-pupil deformable mirror DM1 at a spatial frequency chosen so that this phase is completely converted to amplitude. The phase sinusoid is produced by the pupil deformable mirror, DM3. The control voltages of the introduced aberrations were calculated so that their root mean square value are  $\sigma_{\xi_{up}} = 1.6$  nm and 3.0 nm respectively.

Figure 5 displays the COFFEE and SCC reconstructions of  $\hat{\phi}_u$  along with their Fourier transforms. Figure 6 displays the COFFEE and SCC reconstructions of  $\hat{\xi}_u$  along with their Fourier transforms.

Obviously, the reconstructions are dominated by the introduced phase and amplitude sinusoids, whose Fourier transforms yield spots at the expected locations, matching the spots in the images. The root mean square value of the COFFEE phase reconstruction is 3.0 nm versus 2.9 nm for the SCC one, in excellent accordance with the prescribed value of 3.0 nm. The root mean square value of the COFFEE log-amplitude reconstruction is 1.7 nm versus 1.6 nm for the SCC one, which is also in very good accordance with the prescribed value of 1.6 nm.

The correlation between the COFFEE and the SCC phase estimation is 86%. The correlation between the COFFEE and the SCC log-amplitude estimation is 89%. Several factors contribute to this slight discrepancy in the correlations. While the SCC data are taken with a tip-tilt stabilization loop closed, the COFFEE data had to be taken with the tip-tilt loop open. Consequently, there is a tip-tilt phase difference between the SCC and the COFFEE estimate. Another factor is that there is a sub-pixel centering difference between the COFFEE and the SCC estimates.

### 3. THE NON-LINEAR DARK HOLE TECHNIQUE

#### 3.1 Principle of the non-linear dark hole

Speckle nulling iterative techniques aim at minimizing the energy in a chosen area of the detector in order to facilitate exoplanet detection in this area, called a “Dark Zone” or a “Dark Hole” (DH). To create this DH, the methods developed until recently, which rely on a small aberration approximation, minimize the energy during an iterative process.<sup>6,7</sup> This process requires several iterations and is based on the knowledge of an interaction matrix between the detector plane and the DM pupil plane to create the Dark Hole on the detector.

We have recently proposed a new method to minimize the energy, called non-linear dark hole (NLDH) that does not rely on any small aberration assumption, allowing one to deal for instance with high amplitude phase aberrations such as the ones created by DM dead actuators. Besides, this method takes into account both upstream and downstream aberrations. This compensation method, possibly coupled with COFFEE, would be particularly adapted to the calibration of a high-contrast imaging instrument.



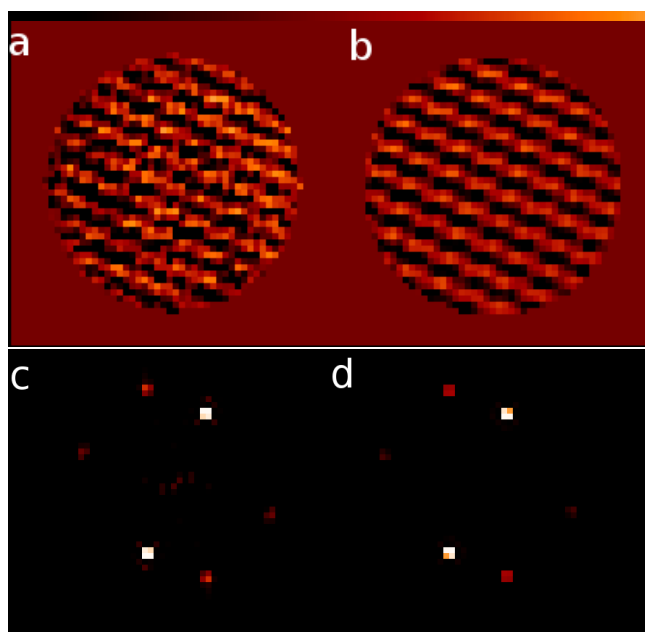


Figure 5. a. Estimated phase using COFFEE (top left). b. estimated phase using the SCC (top right). The linear color bar extends from -8 nm to +8 nm. c. Fourier transform of the estimated phase using COFFEE (bottom left). d. Fourier transform of the estimated phase using the SCC (bottom right). Linear scale.

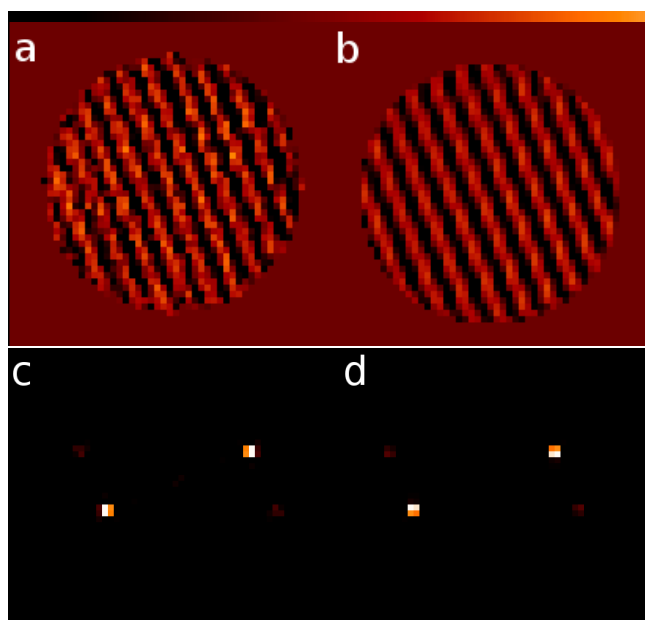


Figure 6. a. Estimated log-amplitude using COFFEE (top left). b. Estimated log-amplitude using the SCC (top right). The linear color bar extends from -4 nm to +4 nm. c. Fourier transform of the estimated log-amplitude using COFFEE (bottom left). d. Fourier transform of the estimated log-amplitude using the SCC (bottom right). Linear scale.

Let us define the energy in the focal plane  $\mathcal{E}_{\text{DH}}$  in the DH as:

$$\mathcal{E}_{\text{DH}} = \iint_{x,y \in \text{DH}} |\Psi_{\text{DH}}(x,y)|^2 dx dy, \quad (6)$$

where  $\Psi_{\text{DH}}(x,y)$  is the complex wavefront on the focal plane, and  $(x,y)$  the position in the DH (for the sake of simplicity, these variables will be omitted in the following). In the latter equation, the squared modulus of the complex wavefront, once integrated on a pixel, and apart from a possible additive background and from a multiplicative factor (which is the star flux in the entrance pupil plane), is nothing but the coronagraphic PSF  $h_c$  of the imaging model of Eq. (1) without a diversity phase but with a correction phase  $\phi_c = F\mathbf{v}$  produced by a pupil-plane DM. We thus re-write the energy in the focal plane  $\mathcal{E}_{\text{DH}}$  in the DH as:

$$\mathcal{E}_{\text{DH}}(\mathbf{v}) = \sum_{(k,l) \in \text{DH}} [\mathbf{h}_{\text{det}} \star \mathbf{h}_c(\phi_u + F\mathbf{v}, \xi_u, \phi_d)](k,l), \quad (7)$$

where  $F$  is the DM's interaction matrix and  $\mathbf{v}$  the vector of applied voltages.

Creating a DH on the detector means finding the set of voltages  $\mathbf{v}_{\text{DH}}$  that minimize the energy  $\mathcal{E}_{\text{DH}}(\mathbf{v})$ , knowing the relationship embodied by  $h_c$  between the entrance pupil plane and the detector plane of the high contrast imaging system, and knowing the wavefront in the former plane (phase  $\phi_u$  and log-amplitude  $\xi_u$ ) and the phase  $\phi_d$  in the downstream pupil plane.

We minimize  $\mathcal{E}_{\text{DH}}(\mathbf{v})$  by means of the same optimization method as the one used by COFFEE to perform its estimation, which is a limited memory variable metric (BFGS) method.<sup>5</sup> Such an operation gives us the voltages  $\mathbf{v}_{\text{DH}}$ , and thus the aberration  $F\mathbf{v}_{\text{DH}}$  to introduce using the DM to create the DH. Unlike others energy minimization methods, the NLDH method does not require a matrix calibration between the detector plane and the DM pupil plane. In particular, if using COFFEE, we are able to estimate the aberrations downstream of the coronagraph, and among them the coronagraphic PSF position on the detector, i.e., the downstream tip-tilt. This estimation is then taken into account in the compensation method (Eq. ((7))). Thus, variation in the aberrations downstream of the coronagraph will not require any particular action during the compensation process, since these variations will be estimated by COFFEE along with the aberrations upstream of the coronagraph.

## 3.2 A precursor to the NLDH: shaping the point spread function on MITHiC

### 3.2.1 Principle and link with the Apodizing Phase Plate

As presented above, the Non-Linear Dark Hole algorithm is able to find the Deformable Mirror shape to apply in order to cancel out the light in a region of the focal plane. This ability includes not only to compensate for phase aberrations, but also to go further and to perform a cancellation of the diffracted light. It means that even with a perfect optical system (without any aberrations), the Non-Linear Dark Hole is able to suppress the diffracted light. As a first validation, we therefore validated the DHNL algorithm experimentally in a non-coronagraphic case on the MITHiC bench in LAM (Marseille). In the absence of a coronagraph, we are not creating a Dark Hole *per se*, but rather performing PSF shaping. This technique, also called Phase Apodized Plate, is by instance used on the METIS instrument for ELT<sup>3</sup> or also in.<sup>8</sup>

### 3.2.2 The MITHiC optical bench

The MITHiC (Marseille Imaging Testbench for High Contrast), shown on Fig. 7, is a bench located in Marseille (LAM) and dedicated to high contrast imaging. More specifically, the purpose of MITHiC is to develop and validate new concepts for high contrast imaging, from new coronagraphic components (Roddier-Roddier coronagraph, with simple and dual zone), to wave-front sensing components (ZELDA mask, phase diversity or COFFEE). The source is monochromatic in the visible, and includes a high order SLM (Spatial Light Modulator) deformable mirror. This device, well suited for laboratory work, requires nevertheless a particular care to the polarisation of the light. MITHiC's source module therefore includes a polarized source ensured by a linear polarizer coupled to a polarisation maintaining monomode fiber. Even though the MITHiC bench includes a coronagraphic mask and a Lyot stop mask, we did not use them for this experiment: we used the CoolSnap imaging camera to perform classical imaging.



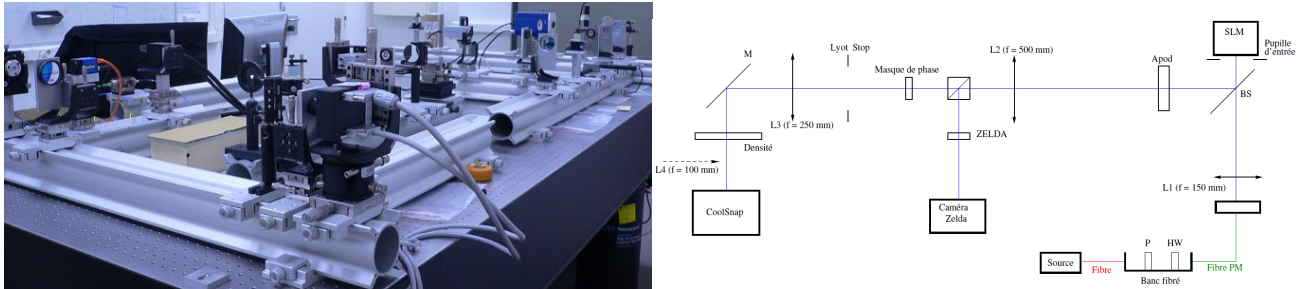


Figure 7. [Left] Picture of the MITHiC bench in LAM. The first element is the SLM, used to modulate the wave-front and generate the Dark Hole on the coronagraph. [Right] scheme of the bench, showing the source module, the SLM, the ZELDA path (unused in the results presented herein), the coronagraph and the imaging camera.

### 3.2.3 Point spread function shaping without a coronagraph on MITHiC

Figure 8 shows the typical optical quality obtained on the MITHiC bench, which is very close to an Airy pattern: the wave-front error level is close to 10nm RMS. In such conditions, the main light residual to be cancelled out comes from diffraction effects, and not from aberrations. This is the context in which we want to test the NLDH on MITHiC. In the absence of a coronagraph, we are not creating a Dark Hole *per se*, but rather performing PSF shaping.

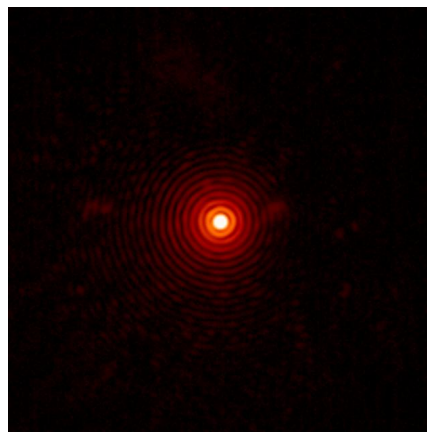


Figure 8. Typical PSF obtained on the MITHiC bench, without a coronagraph. The ghost visible on the right is due to the cube used to perform the beam splitting between ZELDA and imaging path.

We ran the NLDH algorithm to compute the phase to be applied to the SLM in order to cancel the light in a 180 deg half-ring situated on the right side of the PSF, between 2 and 5  $\lambda/D$ . Figure 9 shows, on the left, the PSF after application of the NLDH-computed phase shape on the SLM, and obtained in 1 single iteration. The 180 deg half-ring is clearly visible on the right side. The PSF shape outside of the half-ring is strongly modified, and the Strehl Ratio is of course degraded. On the right of this figure is shown the simulation result of the expected PSF. The PSF shape outside of the half-ring is very similar to what has been obtained on the bench. The contrast level in the dark ring is better in the simulation, which we interpret by the fact that our model of image formation and our model of the DM are not accurate enough. This result is preliminary, and the contrast gain in the Dark Hole area has been estimated to between a factor 3 (at IWA and OWA) to 5 (in the middle of the Dark Hole area). A fine understanding of the limitations in the model should be carried out, and a refined model of the bench and DM should be used to obtain a performance beyond this proof of concept.

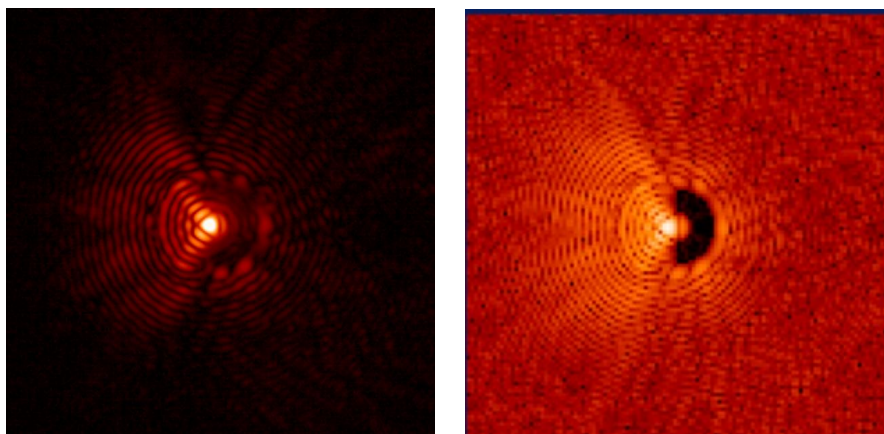


Figure 9. MITHiC's PSF [left] and simulated PSF [right] after applying the Non-Linear Dark Hole technique. The half-ring on the right side of PSF has been attenuated and only shows some residual, witnessing models errors in the bench modelisation and the deformable mirror knowledge.

### 3.3 Coronagraphic simulations of non-linear dark hole

#### 3.3.1 Simulation with perfectly known parameters

In principle, the non-linear dark hole technique finds the optimal control voltages to directly reach the desired contrast, without the need for iterating the procedure if the numerical model of the instrument is good enough.

Figure 10 presents the result of a coronagraphic simulation of contrast optimization with the non-linear dark hole. The simulated instrument is equipped with a four-quadrant phase mask coronagraph, and works with a monochromatic light of wavelength 789 nm. The interaction matrix of the simulated deformable mirror is the best estimate we have of the interaction matrix of the pupil-plane deformable mirror of the THD bench. The upstream phase aberration is a 10 nm (root mean square) aberration whose statistics follows that of the THD bench while performing phase conjugation correction. There is no amplitude aberration. The region where the dark hole will be dug is the bottom half of the image. On the left, the point spread function before application of the non-linear dark hole correction is displayed. The darker central square originates from the chosen spectrum density, representative of good but not perfect phase conjugation inside the corrected zone of the deformable mirror. On the right, the point spread function after application of the non-linear dark hole correction is displayed. The calculation for this dark hole correction took less than a minute on a standard desktop computer equipped with a processor with a 2.80 GHz frequency. In this particular case, the contrast in the dark hole zone goes from  $2.4 \times 10^{-7}$  to  $1.2 \times 10^{-8}$ .

#### 3.3.2 Simulation with an error on the aberration estimation

Since the non-linear dark hole is entirely model-based, trouble may arise if there are discrepancies between the parameters of the model and the real experiment that it is supposed to represent. One of the possible sources of discrepancy is the measurement of the aberrations. We show on Fig. 11 the result of a simulation where the true phase aberration differs from the measured aberration by a 1 nm root mean square aberration whose statistics follows the same energy spectrum density as the true phase aberration.

Figure 12 shows a zoom on the dark hole region. On the left is displayed the dark hole when the phase is perfectly known, on the right is displayed the dark hole when the phase is imperfectly known. Although the difference is not very high, it accounts for a contrast of  $1.4 \times 10^{-8}$  instead of  $1.2 \times 10^{-8}$  in the error-free case.

#### 3.3.3 Simulation with an error on the influence matrix of the deformable mirror

Another possible source of discrepancy is an imprecise knowledge of the influence matrix of the deformable mirror. We show on Fig. 13 the result of a simulation where the level of response of each of the actuators of the deformable differ from the description of the interaction matrix. For each actuator, the level of response differs

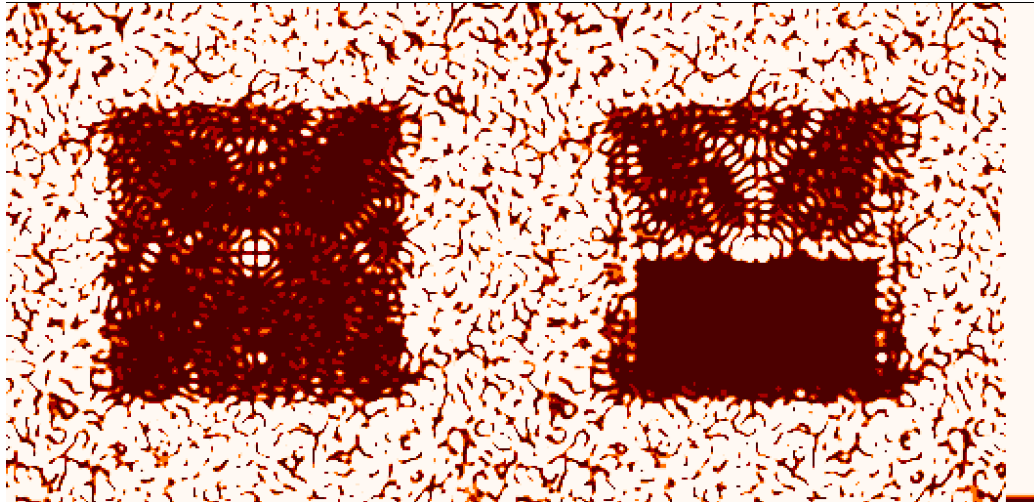


Figure 10. Left: coronagraphic point spread function before non-linear dark hole correction (simulation). Right: coronagraphic point spread function after non-linear dark hole correction (simulation). The scale is an argument hyperbolic sine, which is similar to a logarithmic scale. The color bar is on the right.

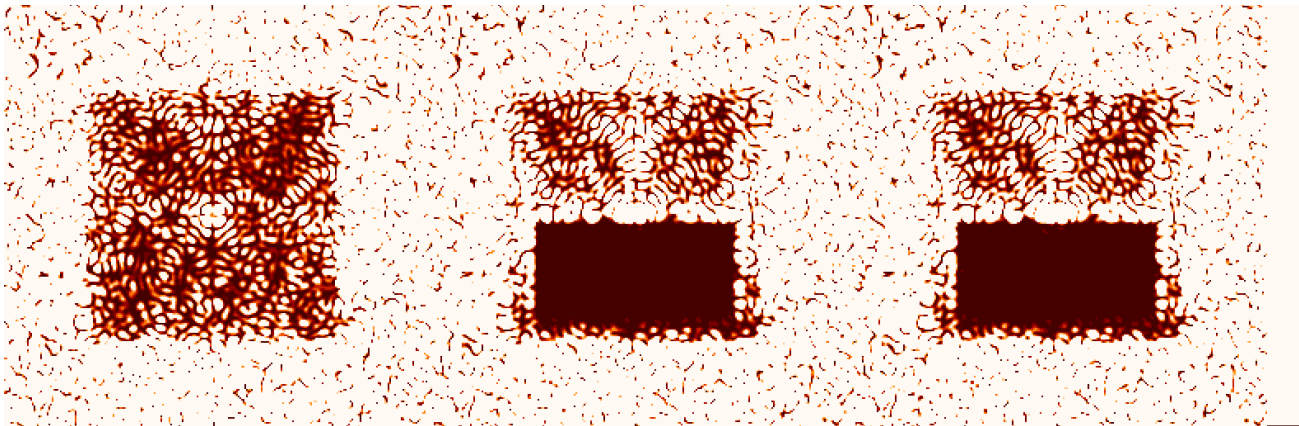


Figure 11. Left: coronagraphic point spread function before non-linear dark hole correction (simulation). Middle: coronagraphic point spread function after non-linear dark hole correction with a perfectly known phase (simulation). Right: coronagraphic point spread function after non-linear dark hole correction with an imperfectly known phase (simulation). The scale is an argument hyperbolic sine.

from the supposed response by a realization of a centered random Gaussian variable with standard deviation 0.05. In these simulations, there is no error on the phase estimate. In this case, there are obvious speckles in the corrected zone.

Figure 14 shows a zoom on the dark hole region. On the left is displayed the dark hole when the interaction matrix is perfectly known, on the right is displayed the dark hole when the interaction matrix is imperfectly known. In this case, the difference is much higher: it accounts for a contrast of  $7.1 \times 10^{-8}$  instead of  $1.2 \times 10^{-8}$  in the error-free case.

### 3.3.4 Simulation with an error both on the aberration estimation and on the influence matrix of the deformable mirror

To get a better idea on how the sources of error combine, we show on Fig. 15 the result of a simulation where there are errors both on the phase estimate and the interaction matrix. Speckles are again clearly visible in the dark hole of the rightmost image.

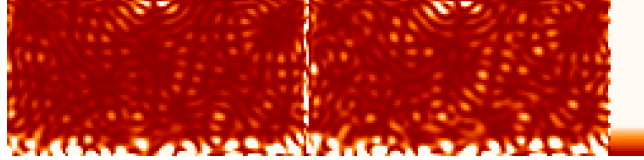


Figure 12. Left: dark hole obtained with a perfectly known phase. Right: dark hole obtained with an imperfectly known phase. The scale is linear.

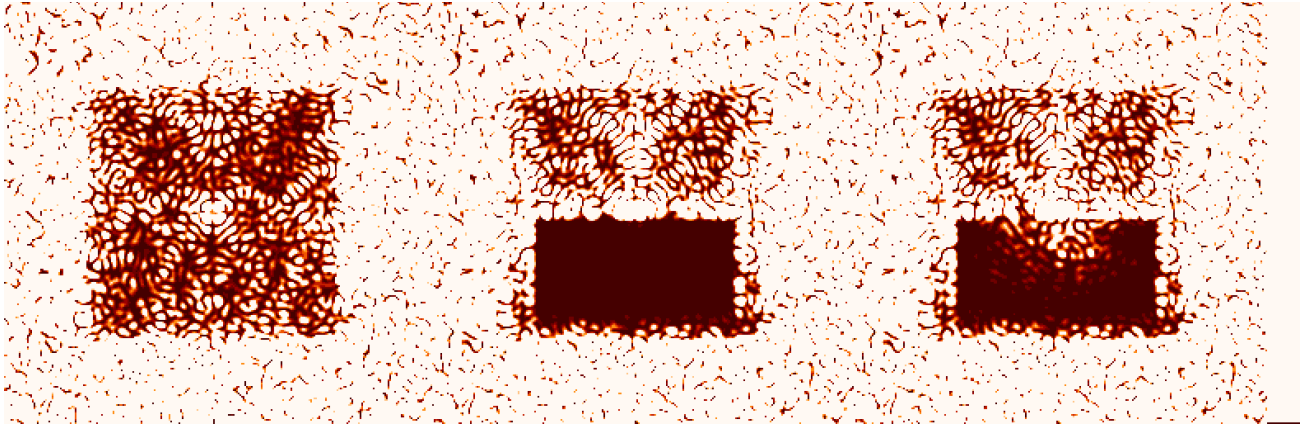


Figure 13. Left: coronagraphic point spread function before non-linear dark hole correction (simulation). Middle: coronagraphic point spread function after non-linear dark hole correction with a perfectly known interaction matrix of the deformable mirror (simulation). Right: coronagraphic point spread function after non-linear dark hole correction with an imperfectly known interaction matrix (simulation). The scale is the same as Fig. 11.

Figure 16 shows a zoom on the dark hole region. On the left is displayed the dark hole when both the phase and the interaction matrix are perfectly known, on the right is displayed the dark hole when the phase and interaction matrix are imperfectly known. In this case, the contrast in the dark hole is  $7.2 \times 10^{-8}$  instead of  $1.2 \times 10^{-8}$  in the error-free case, and  $7.1 \times 10^{-8}$  when there is an error on the interaction matrix, but no error on the phase.

We conclude that the precision on the knowledge of the interaction matrix of the deformable mirror must be very high. Imperfect calibration of the deformable mirror might be the highest source of errors. The errors due to imprecisions in the knowledge of the interaction matrix might be more severe if the shape of the response of individual actuators is unknown. Interestingly, the loss of performance due to imprecise knowledge on the behaviour of the deformable mirror seems to be independent of the loss of performance due to imperfect estimation of the wavefront.

### 3.4 Experimental validation of the non-linear dark hole on the THD bench

We performed a preliminary experimental validation of the non-linear dark hole on the THD bench. We started in a configuration where a pupil-plane mirror and an off-pupil-plane mirror are used to obtain a region of maximal

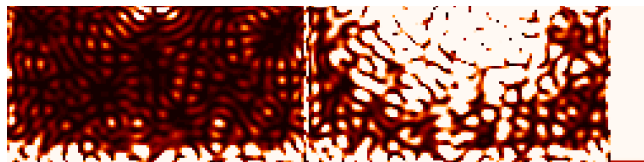


Figure 14. Left: dark hole obtained with a perfectly known interaction matrix. Right: dark hole obtained with an imperfectly known interaction matrix. The scale is linear.



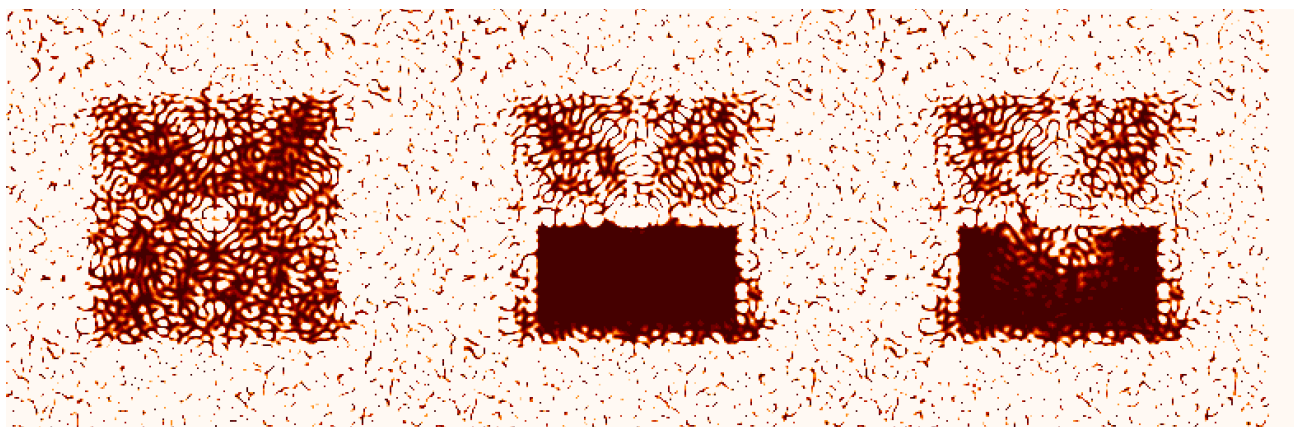


Figure 15. Left: coronagraphic point spread function before non-linear dark hole correction (simulation). Middle: coronagraphic point spread function after non-linear dark hole correction with perfectly known phase and interaction matrix of the deformable mirror (simulation). Right: coronagraphic point spread function after non-linear dark hole correction with an imperfectly known interaction matrix and an error on the phase estimate (simulation). The scale is the same as Fig. 11.

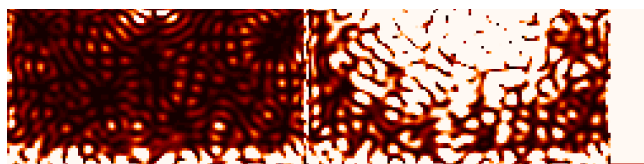


Figure 16. Left: dark hole obtained with a perfectly known phase and interaction matrix. Right: dark hole obtained with an imperfectly known phase and interaction matrix. The scale is linear.

contrast inside the zone within reach of correction of the deformable mirrors.<sup>9</sup> The corresponding point spread function is the leftmost image of Fig. 17.

At this point, a measurement using the self-coherent camera is used to retrieve both the residual phase and amplitude aberrations on the bench. The self-coherent camera estimates are expressed in a focal plane. Since the current implementation of the non-linear dark hole needs phase and amplitude estimates to be expressed in the entrance pupil plane, the self-coherent camera estimates are backpropagated to the entrance pupil plane. These aberrations, along with a model of the THD bench, are taken as input parameters for the non-linear dark hole method. The output of the non-linear dark hole program is the set of control voltages that must be added to the pupil-plane deformable mirror in order to optimize the contrast in the bottom half of the focal plane. The resulting point spread function is the second from the left in Fig. 17. A linear-scale zoom of the dark hole region is displayed in Fig. 18.

However, the numerical model of the THD is not perfect. In the context of phase diversity, some two to three iterations are usually needed to reach the minimum.<sup>10</sup> For this reason, and even though it would be unnecessary if the numerical model were perfect, we repeat the procedure four times (which amounts to a total of five corrections): we retrieve the current phase and amplitude aberrations; we use them as input of the non-linear dark hole program; and we use the new control voltages.

Figure 19 displays the contrast in the dark hole as a function of the number of correction steps. It converges in three iterations, then saturates without divergence.

For clarity, Figs 17 and 18 display only the image before correction and the result of the four first iteration of correction – the fifth iteration is indistinguishable from the fourth.

There is a clear effect of the the non-linear dark hole commands when going from iteration 0 (the image in the initial situation) to iteration 1. The dark hole zone then becomes a bit cleaner each time. The error is mainly



Figure 17. From left to right: point spread function before NLDH correction, after 1 correction, after 2 corrections, after 3 corrections, and after 4 corrections. Argument hyperbolic sine scale.

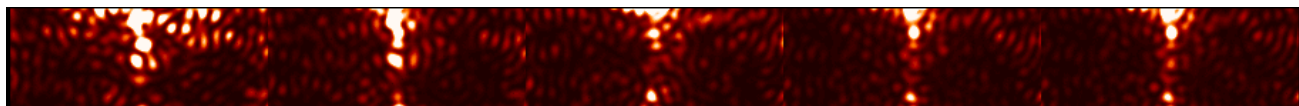


Figure 18. From left to right: point spread function before NLDH correction, after 1 correction, after 2 corrections, after 3 corrections, and after 4 corrections. Linear scale.

localized on the axis, with a few weak speckles out of the axis too. There are probably several causes for the residual starlight.

Firstly, the residual speckles on the axis are uncorrected by the non-linear dark hole because they are unseen by the model of the four-quadrant phase mask coronagraph. Indeed, the numerical model of this coronagraph is insensitive to aberrations whose signature in the image lies on the horizontal and vertical axes (see, <sup>1</sup> appendix A). Hence, getting rid of these aberrations is particularly difficult.

Secondly, the backpropagation of the self-coherent camera estimates to the entrance pupil plane is an ill-posed problem, and it is likely to be a source of errors. We plan on using two different solutions to this issue. On the one hand, using COFFEE as a wavefront sensor would provide pupil-plane estimation in a very natural way. On the other hand, we could improve the backpropagation of the aberrations estimate from the focal plane of the detector to the entrance pupil plane.

Finally, the interaction matrix of the deformable mirror is not perfectly known, and we suspect it could also

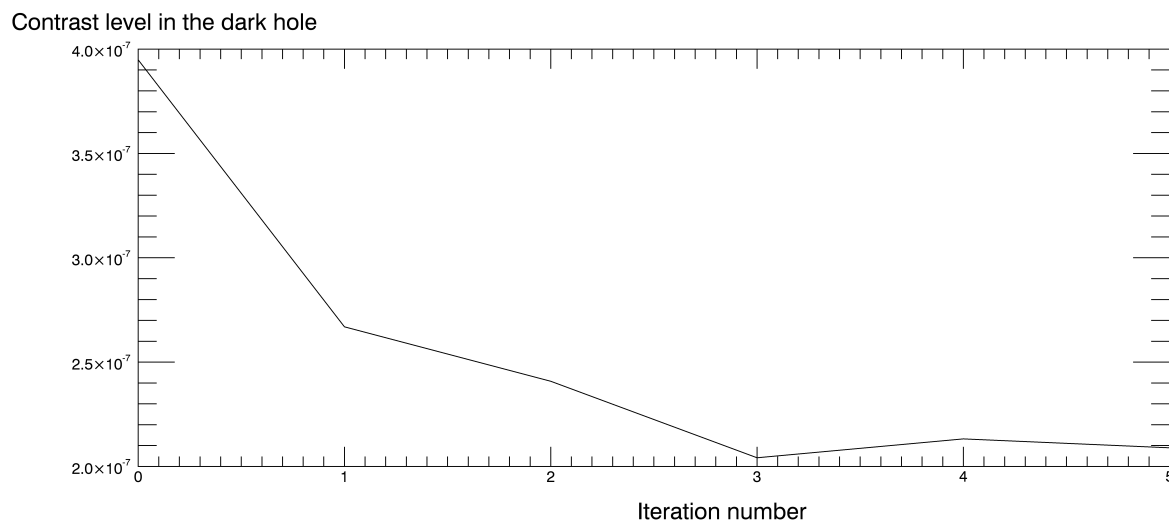


Figure 19. Contrast in the dark hole as a function of the number of correction steps



contribute to the error, as suggested by the simulations.

#### 4. CONCLUSION

In this communication we have tackled two problems of high-contrast imaging for space missions. Firstly we have shown that COFFEE, the coronagraphic phase diversity, is able to reconstruct jointly phase and amplitude aberrations with a very good precision, which is necessary to reach very high contrasts. Secondly we have performed the first preliminary experimental validation of the non-linear dark hole technique and proven the validity of the concept, as well as the fast convergence in two to three iterations. The absolute performance is currently limited by various factors, inaccuracies in the numerical models of the instrument being the most critical. Numerical simulations have allowed us to explore the impact of model errors on the quality of the resulting dark hole. Nevertheless, the current performance already suggests that the non-linear dark hole can be a fast and efficient technique for space-based exoplanet imaging missions. Future work will include furthering the precision of the calibration of the experimental testbed, more sophisticated algorithms, and testing the coupling of COFFEE estimation to non-linear dark hole creation.

#### ACKNOWLEDGMENTS

The PhD work of O. Herscovici-Schiller is co-funded by CNES and ONERA. This work received funding from the E.U. under FP7 Grant Agreement No. 312430 OPTICON, from CNES under contract 4500053798/DIA094, from the CNRS (Défi Imag'In) and from ONERA in the framework of the VASCO research project.

#### REFERENCES

- [1] Herscovici-Schiller, O., Mugnier, L. M., Baudoz, P., Galicher, R., Sauvage, J.-F., and Paul, B., “Experimental validation of joint phase and amplitude wave-front sensing with coronagraphic phase diversity for high-contrast imaging,” *Astronomy and Astrophysics (accepted)* (2018).
- [2] Paul, B., Mugnier, L. M., Sauvage, J.-F., Dohlen, K., and Ferrari, M., “High-order myopic coronagraphic phase diversity (COFFEE) for wave-front control in high-contrast imaging systems,” *Opt. Express* **21**(26), 31751–31768 (2013).
- [3] Kenworthy, M. A., Codona, J. L., Hinz, P. M., Angel, J. R. P., Heinze, A., and Sivanandam, S., “First on-sky high-contrast imaging with an apodizing phase plate,” *The Astrophysical Journal* **660**(1), 762 (2007).
- [4] Mugnier, L. M., Fusco, T., and Conan, J.-M., “Mistral: a myopic edge-preserving image restoration method, with application to astronomical adaptive-optics-corrected long-exposure images,” *J. Opt. Soc. Am. A* **21**, 1841–1854 (Oct 2004).
- [5] Thiébaud, É., “Optimization issues in blind deconvolution algorithms,” in [*Astronomical Data Analysis II*], Starck, J.-L. and Murtagh, F. D., eds., **4847**, 174–183, Proc. Soc. Photo-Opt. Instrum. Eng. (Dec. 2002).
- [6] Bordé, P. J. and Traub, W. A., “High-Contrast Imaging from Space: Speckle Nulling in a Low-Aberration Regime,” *The Astrophysical Journal* **638**(1), 488 (2006).
- [7] Give'on, A., Belikov, R., Shaklan, S., and Kasdin, J., “Closed loop, DM diversity-based, wavefront correction algorithm for high contrast imaging systems,” *Opt. Express* **15**, 12338–12343 (Sep 2007).
- [8] Carlomagno, B., Absil, O., Kenworthy, M., Ruane, G., Keller, C., Otten, G., Feldt, M., Hippler, S., Huby, E., Mawet, D., Delacroix, C., Surdej, J., Habraken, S., Forsberg, P., Karlsson, M., Catalan, E., and Brandl, B., “End-to-end simulations of the e-elt/metis coronagraphs.”
- [9] Mazoyer, J., Baudoz, P., Galicher, R., and Rousset, G., “High-contrast imaging in polychromatic light with the self-coherent camera,” *A&A* **564**, L1 (2014).
- [10] Paul, B., Sauvage, J.-F., Mugnier, L. M., Dohlen, K., Petit, C., Fusco, T., Mouillet, D., Beuzit, J.-L., and Ferrari, M., “Compensation of high-order quasi-static aberrations on SPHERE with the coronagraphic phase diversity (COFFEE),” *A&A* **572**, A32 (2014).